Journal Pre-proof

Investigating mass transfer around spatially-decoupled electrolytic bubbles

Akash Raman, Carla Corina dos Santos Porto, Han Gardeniers, Cíntia Soares, David Fernández Rivas, Natan Padoin

Please cite this article as: A. Raman, C.C. dos Santos Porto, H. Gardeniers et al., Investigating mass transfer around spatially-decoupled electrolytic bubbles, *Chemical Engineering Journal* (2023), doi: https://doi.org/10.1016/j.cej.2023.147012.

This is a PDF file of an article that has undergone enhancements after acceptance, such as the addition of a cover page and metadata, and formatting for readability, but it is not yet the definitive version of record. This version will undergo additional copyediting, typesetting and review before it is published in its final form, but we are providing this version to give early visibility of the article. Please note that, during the production process, errors may be discovered which could affect the content, and all legal disclaimers that apply to the journal pertain.
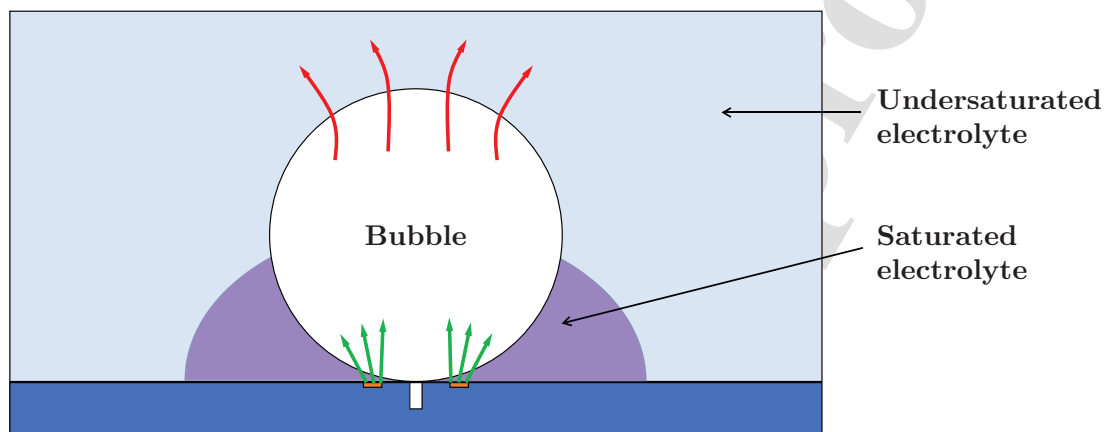
1 Graphical Abstract

2 **Investigating Mass Transfer Around Spatially-Decoupled Electrolytic Bubbles**

3 Akash Raman, Carla Corina dos Santos Porto, Han Gardeniers, Cíntia Soares, David Fernández

4 Rivas, Natan Padoin

Investigating Mass Transfer Around Spatially-Decoupled Electrolytic Bubbles

Akash Raman[a,*], Carla Corina dos Santos Porto[b], Han Gardeniers[a], Cíntia Soares[b,*], David Fernández Rivas[a], Natan Padoin[b]

[a]Mesoscale Chemical Systems Group, MESA+ Institute for Nanotechnology, Faculty of Science and Technology, University of Twente, P.O. Box 217, Enschede, 7500 AE, The Netherlands
[b]Laboratory of Materials and Scientific Computing - LabMAC, School of Technology, Federal University of Santa Catarina (UFSC), 88040-900, Florianópolis/SC, Brazil

Abstract

Electrolytic bubbles have a profound impact on mass transport in the vicinity of electrodes, greatly influencing the electrolyzer efficiency and cell overpotential. However, high spatio-temporal resolution experimental measurements of concentration fields around electrolytic bubbles, are challenging. In this study, a succession of spatially-decoupled electrolytic bubbles growing in a initially quiescent electrolyte is simulated. The bubbles grow, and departing from a hydrophobic cavity at the center of a ring microelectrode. The gas-liquid interface is modeled using a moving mesh topology. A geometric cutting protocol is developed to handle topology changes during bubble departure. The simulated bubbles show good agreement with the bubble growth dynamics observed in experiments. The bubbles in this spatially-decoupled system outgrow the region of electrolyte that is saturated with dissolved hydrogen. This leaves the apex of the bubble interfaces exposed to an undersaturated region of the electrolyte which leads to an outward flux of hydrogen gas. This is shown to limit the gas evolution efficiency of bubbles despite the fact that they grow at a constant volumetric rate. By analyzing the distribution of the flux of dissolved hydrogen along the bubble interface along with the development of dissolve hydrogen concentration profiles around the bubble, we show that the magnitude of the outward diffusive flux at the apex of the bubble decreases with increasing electrolysis current.

---

*Corresponding author.
Email addresses: a.raman@utwente.nl (Akash Raman), cintia.soares@ufsc.br (Cíntia Soares)

numerical simulation, moving mesh

1. Introduction

The decarbonization of industries is a key step in reaching net-zero carbon emissions and low-carbon hydrogen is expected to play a key role in this transition [20]. Water electrolysis offers a robust way to generate clean hydrogen for industrial, and commercial applications while also raising the possibility of offsetting the intermittency of renewable energy sources [1, 38]. As a result, water electrolysis driven by renewable energy sources is expected to meet $\sim 38\%$ of global hydrogen demand by 2030 [21].

Gas bubbles nucleate on the surface of electrodes during gas-evolving electrochemical reactions such as water electrolysis. These electrolytic bubbles are known to greatly influence the transport of dissolved product gases, as well as the transport of ionic species, in the vicinity of the electrode [4]. Electrolytic bubbles are a significant source of inefficiency in electrolyzers. They increase the electrical resistance in electrolyzers by restricting ion conduction pathways in the electrolyte, and by covering portions of the electrode and rendering them inactive [4, 5, 13, 28, 60, 63]. However, bubbles can also lower the concentration of dissolved gases, and induce microconvective flows - effects known to have a positive influence on electrolysis [27, 40, 41, 43, 62, 64]. Despite the sustained interest in electrolytic bubbles, the scientific problem of the optimal bubble management remains open [25]. It has been suggested that the optimization of bubble evolution phenomena can lead to a 5-10 % improvement in electrolysis stack efficiency [52]. Therefore, advancing our understanding of electrolytic bubbles is important in the context of global climate change mitigation.

Several publications on the topic have focused on studying the nucleation, growth and departure dynamics of electrolytic bubbles under varying conditions [9, 11, 16, 22, 29, 35, 41, 43, 45, 47, 49, 57, 58, 61, 66, 68, 70]. However, the design of next-generation electrodes with optimized bubble evolution characteristics requires greater understanding of the evolution of the concentration profile of dissolved gas in the vicinity of the bubbles. Advances in high

speed imaging techniques, and confocal microscopy have opened up possibilities to observe bubble-related phenomena with much greater spatio-temporal resolution than before [33]. Scanning probe techniques such as scanning electrochemical microscopy (SECM) have been used to measure local dissolved gas concentrations in the vicinity of bubbles [15, 31, 32, 65]. However, the presence of the SECM probe, and its movement during raster scans can influence the concentration profile and disrupt natural convective flows. Recent studies have applied confocal fluorescence microscopy to study variations in pH around electrolytic bubbles [26, 39]. The development of new fluorescent probes for fluorescence lifetime imaging microscopy also open up new possibilities in this direction [8]. Nevertheless, the direct experimental measurement of the concentration gradients in three dimensions surrounding electrolytic bubbles remains a challenge due to the presence of complex convective flows, and the fast growth of the bubbles in comparison to the timescales required by analytical techniques. Several studies have attempted to fill this gap in knowledge through the use of direct numerical simulations (DNS) which can offer the necessary spatio-temporal resolution required to understand electrolytic bubble evolution across length scales.

Vachaparambil and Einarsrud [55] simulated the growth of a rising bubble in a supersaturated medium using the volume of fluid (VOF) model. The compressive continuous species transfer model, the sharp surface force model, the driving force for the bubble growth (Fick's first law and a mass transfer correlation), as well as the relevant source terms, were implemented in the open source code OpenFOAM 6. The authors validated their numerical predictions against theoretical models (Epstein–Plesset, Scriven, and Extended Scriven).

This VOF-based framework was further extended by the respective authors to account for single, and dual bubble growth, and departure, considering coalescence in the latter case [56]. The authors considered a coupling of multiphase flow, electrochemical reactions, species and charge transport, and interfacial mass transfer in their simulations. The model was verified with analytical models for bubble growth in supersaturated medium, steady bubble, and rising bubble.

4

Other studies have used the VOF method to simulate interface-resolved growth, and in some cases departure and rise, of electrolytic bubbles [30, 73]. However, different alternatives are available for multiphase modeling, as highlighted by Taqieddin et al. [54]. Of the interface capturing methods, phase-field [18, 34] and level-set [51, 71] are also relevant. While they are less precise than moving mesh in the computation of the fluxes across the interface, they allow topology changes - a significant advantage for simulating bubble departure from a surface.

Using a sharp interface immersed boundary method and artificial compressibility for the pressure, Khalighi et al. [24] studied the growth of a single hydrogen bubble attached to a vertical cathode in a narrow channel under forced convection conditions. The authors solved the Navier-Stokes equations, as well as the species balance and potential equations. The effect of the fluid flow rate and the operating pressure was evaluated, considering the bubble growth behavior, species concentration, potential, and current density as dependent variables. Although a rigorous numerical analysis was carried out, the results were not compared to experimental data or analytical models, and bubble departure was not considered.

Other studies have also considered the influence of variations in physical properties, e.g., density and surface tension, due to thermal and solutal gradients. Sepahi et al.[48] used the immersed boundary method to study the growth of single and multiple hydrogen bubbles in acidic water electrolysis and compared their theoretical predictions with experimental data. The authors found a significant effect of buoyancy-driven convection on the bubble dynamics. Moreover, investigations about Marangoni convection due to thermo-, and solutal-capillary effects have also been reported [36, 37, 69]. Using a finite element method-based solver, Meulenbroek et al. [37] investigated the formation of Marangoni forces that retarded the departure of electrolytic hydrogen bubbles. A stagnant cap formed by compression of surfactants at the apex of the bubble, suppressing motion in that portion, was considered in the simulations, either specifying a stagnation angle at the interface or calculating the dynamic formation of this region. However, a mobile interface was considered at the bottom

5

91 of the bubble, where Marangoni flow causes the formation of vortices.

92 Furthermore, several contributions on the simulation of multiple bubbles generated by

93 hydrogen evolution from water electrolysis in larger electrodes using Euler-Euler and Euler-

94 Lagrange formulations can also be found in literature [10, 14, 19, 44, 50, 53, 67, 72]. Such

95 approach do not consider the gas-liquid interface explicitly, but are well-suited for the in-

96 vestigation of the effect of electrolytic bubbles on the performance of electrolyzers on a

97 macro-scale.

98 The vast majority of studies on electrolytic bubbles consider the formation of the bubbles

99 directly atop the electrode surface. An exception to this is the study by Peñas et al. [41]

100 which investigated the evolution of hydrogen bubbles from a hydrophobic microcavity away

101 from a ring microelectrode surface, spatially decoupling the site of bubble nucleation from

102 the site of water electrolysis. The study considered experiments, and a simplified numerical

103 model that allowed a qualitative understanding of the effect of bubble evolution on the

104 concentration, and Ohmic overpotential. A subsequent analysis of bubble growth, and its

105 influence on the half-cell potential in this decoupled electrolysis system was performed with

106 the aid of a simplified numerical model which calculated the change in Ohmic resistance

107 in the system as a function of bubble radius [43]. This combination of experiments and

108 modeling showed the precise influence of bubbles on the concentration overpotential. The

109 bubble was considered a fixed domain, and bubble departure was not explicitly considered

110 in the aforementioned studies considering spatially decoupled electrolysis.

111 In this paper, we present a detailed DNS investigation of convective, and diffusive mass

112 transfer around single, successive, spatially-decoupled electrolytic bubbles growing in the

113 superhydrophobic pit-ring system in the absence of forced electrolyte convection. The adop-

114 tion of an arbitrary Lagrangian-Eulerian (ALE) moving mesh method allowed the detailed

115 quantification of the fluxes at the bubble interface. Since the ALE moving mesh method

116 cannot handle topology changes, an interface cutting protocol was developed to re-initialize

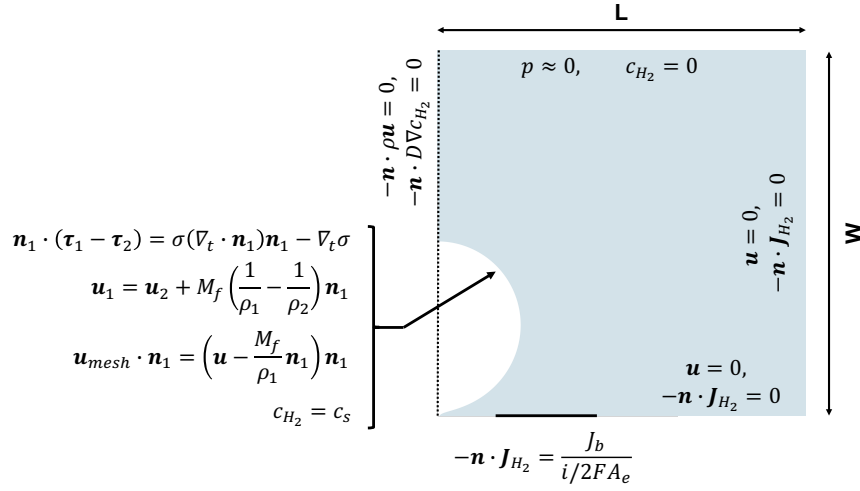117 the simulation during bubble departure. Herein, we simulate larger bubbles than the ones

6

Figure 1: A schematic representation of the 2D axisymmetric model geometry. The bubble is depicted as a white semicircle. The ring electrode is shown as the solid black line at the bottom. The boundary conditions specified in the geometry are indicated. The axis of symmetry is the left edge of the schematic indicated by the dotted line.

commonly reported in the literature, which grow beyond the concentration boundary layer. The time-dependent investigation considering coupled fluid flow and mass transfer is presented, which represents a significant advancement regarding the study of Peñas et al. [41]. The model results are validated against experimental findings from [43] and offer insight into the evolution of the concentration field in the vicinity of the bubble, and the electrode. The model is then used to shed light on the effect of the distance between the site of electrolysis (the ring electrode), and the site of bubble nucleation (the superhydrophobic cavity).

2. Numerical simulation setup and methodology

The numerical simulations were performed in a 2D axisymmetric domain with the finite element-based solver COMSOL$^\circledR$ Multiphysics (Burlington MA, USA). The computational domain, highlighting the dimensions and the location of the boundary conditions, is depicted in detail in Fig. 1. The numerical model was designed to closely resemble the experimental system in which electrolytic bubbles nucleate, grow, and depart from a hydrophobic cavity or radius $r_p = 10$ μm surrounded by a ring electrode of inner radius $R_{in} = 230$ μm , and

132 outer radius $R_o = 255$ μm. The computational geometry consists of a 7 mm × 7 mm

133 rectangular domain. The incipient bubble was described as a quadrant of radius r_p centered

134 at the geometric origin. The electrode was described as a line segment on the r-axis between

135 $r = R_{in}$, and $r = R_o$.

136   Additional rectangular subdomains were defined in order to prescribe finer meshing pa-

137 rameters around the bubble, and around the electrode surface. First, a 2 mm × 1.2 mm

138 rectangular subdomain was built starting from the origin to allow the discretization with a

139 finer mesh in the region of the greatest mesh deformation during the bubble growth phase.

140 In the bubble rise phase, the height of this rectangular subdomain was extended to the top

141 of the geometry by creating a 7 mm × 1.2 mm rectangular subdomain. Second, a 45 μm× 10

142 μm rectangular subdomain was built around the electrode to ensure greater mesh refinement

143 in order to better capture the steep concentration gradients in this region.

144   The entire domain was initially discretized with a non-structured mesh consisting of

145 approximately 9×10^4 elements. A finer mesh was imposed also at the bubble interface

146 throughout the entire simulations, ensuring a proper resolution independently of the bubble

147 size. Moreover, a mesh refinement study was carried out to ensure that the final mesh

148 produced independent results throughout the entire run. All initial meshing parameters

149 are described in the supplementary information (see SI Sec. S1.1). Remeshing was needed

150 throughout the simulation to ensure proper mesh refinement as the bubbles grow or rise.

151 A maximum mesh distortion threshold (see SI Sec. S1.1), with backward Euler consistent

152 initialization, was considered in all cases.

153   Pure water and hydrogen at room conditions were considered as the liquid and gas phases,

154 respectively. The diffusivity of H_2 in water was fixed at 5×10^{-9} m^2·s^{-1} in all simulations

155 [59]. Since the currents considered in the study were ≤ 50 μA , no appreciable changes in

156 the temperature of the electrolyte were expected. As a result, isothermal conditions were

157 assumed in all cases, and the temperature was fixed as T = 300 K. The Henry's constant

158 of H_2 , $k_H = = 7.7 \times 10^{-6}$ mol·m^{-3} was considered in all simulations [46]. The electrolyte
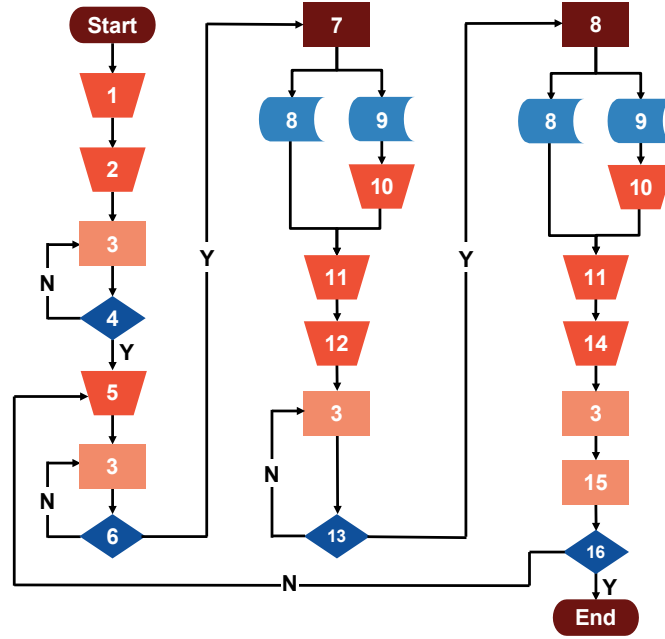
8

Figure 2: Numerical procedure flowchart. (1) Initialization of geometry, mesh, initial conditions, boundary conditions and remeshing parameters. (2) Setting up a time-dependent boundary condition at the bubble interface. (3) Solving mass, momentum, and species balance equations. (4) Checking if $t \geq t_s$ where t_s is the time taken for the electrolyte to become saturated at the bubble nucleation site with a stationary (non-growing) bubble. (5) Boundary condition at the bubble interface is a constant value of $c = c_s$ where c_s is the saturation concentration. (6) Checking if the bubble neck radius has reached the threshold, $r_{min} \leq 20$ nm. (7) Stopping the calculation. (8) Saving the current mesh. (9) Saving the flow variables (velocity components, pressure, and concentration). (10) Replacing voids by c_s. (11) Importing and interpolating the flow variables into a new simulation setup. (12) Enforcing bubble departure. (13) Checking if $z_{max,rising} < z_{threshold}$. (14) Removing the rising bubble. (15) Incrementing the bubble count (N). (16) Checking if $N > N_{total}$.

9

159 was equilibriated with the atmosphere before, and during the experiments. Thus, a uniform

160 initial concentration of $c_i = 3.85 \times 10^{-7}$ mol·m^{-3} (considering 0.5 ppm of H$_2$ in air [17]), and

161 quiescent conditions ($\mathbf{u} = 0$) were specified throughout the electrolyte domain.

162 A time-dependent profile was specified for the H$_2$ concentration at the bubble interface

163 for the first bubble. The concentration at the bubble-electrolyte boundary was increased

164 from c_i at the beginning of the simulation, to the saturation concentration of H$_2$, $c_s = 0.77$

165 mM at the saturation time t_s. The saturation time, t_s is the time taken for the saturation

166 of the electrolyte layer immediately adjacent a stationary (non-growing) bubble interface at

167 the hydrophobic cavity. The concentration profile, and t_s were approximated based on a

168 preliminary simulation without the moving mesh topology; i.e., the preliminary simulation

169 only considered the diffusion of hydrogen from at the ring electrode surface to the surface

170 of a stationary bubble. Details of the preliminary simulation, and the concentration profiles

171 used for the time-dependent boundary condition are presented in SI Sec. S1.4. Following the

172 initial ramp, a constant concentration equal to c_s was maintained at the bubble interface for

173 the remainder of the simulation. Furthermore, the time-dependent concentration boundary

174 was not applied to subsequent bubbles which nucleate within a saturated region of the

175 electrolyte.

176 It is worth noting that the ramp in concentration of hydrogen in the bubble also occurs

177 in experiments. The superhydrophobic cavity remains filled with ambient air (and not hy-

178 drogen) when the electrolyte is added. At the onset of electrolysis, after the saturation of

179 the electrolyte with hydrogen, the concentration of hydrogen in the cavity increases. This

180 was represented in the simulations by means of a time-dependent concentration boundary

181 condition at the bubble interface. The time-dependent ramp was also necessary because

182 the electrolyte surrounding the gas cavity is initially undersaturated, and a time-invariant

183 boundary condition of $c = c_s$ would cause the bubble to shrink.

184 The mathematical model consisted of a set of nonlinear partial differential equations

185 describing the fluid flow and the H$_2$ transport within the computational domain. While

10

the fluid flow equations were solved in all subdomains (liquid and gas), the H_2 transport equation was solved only in the liquid phase. Section 2.1 presents the details of the mathematical model solved herein. The balance equations (momentum and species transport) were solved with the direct MUltifrontal Massively Parallel Solver (MUMPS) [2, 3]. Moreover, the Backward Differentiation Formula (BDF) solver was used for calculating the time step [7].

In all models, the electrolysis current was specified as a constant flux of H_2 at the ring electrode's surface (see SI Sec. S1.3). The bubble grows due to H_2 transport across the interface, which was calculated by integrating the H_2 diffusive flux weighted by the molecular weight of H_2 along the bubble interface. The calculation was stopped when the neck radius r_{min}, which was measured as the minima of the radial coordinate along the bubble interface, falls below a threshold $r_{min} \leq 20$ nm.

Then, the mesh and the flow variables (velocity components, pressure, and concentration) were exported for the simulation of the departure of the bubble from the hydrophobic cavity, and its subsequent rise through the bulk of the electrolyte. The same initial meshing and remeshing parameters considered in the bubble growth step were adopted. Therefore, the flow variables were interpolated in the initial mesh generated for the bubble departure and rising step. However, since the species transport equations were not solved in the bubble domain, voids in the concentration matrices were replaced by the H_2 saturation concentration ($c_s = 7.7 \times 10^{-6}$ mol·m^{-3}) for consistency.

Moreover, since the implementation of the moving mesh model considered herein does not allow topological change, the departure event was implemented by altering the model geometry and splitting the single bubble domain into a rising bubble, and an incipient cap pinned to the hydrophobic cavity. The position of the bubble neck was identified as the minima of the radial coordinate along the bubble interface, and the region was cut by removing a 5 μm tall rectangular portion (see SI Sec. S1.5), resulting in a separation between the interface of the rising bubble and the interface of the bubble remaining at the pit.

11

²¹³ The bubble rising event was simulated until the bubble interface reached a distance
²¹⁴ of 200 μm from the upper boundary of the computational domain. Then, the mesh and
²¹⁵ the data at the last time step were exported. A new simulation was initialized with the
²¹⁶ exported topology and variables. In the setup for the simulation of the second bubble growth,
²¹⁷ the bubble at the top of the computational domain was removed. The initial mesh and
²¹⁸ remeshing parameters were also the same mentioned earlier. Therefore, the imported flow
²¹⁹ variables (velocity components, pressure, and concentration) were interpolated throughout
²²⁰ the elements of the current mesh, considering a replacement of the voids in the matrix by
²²¹ the H_2 saturation concentration ($c_s = 7.7 \times 10^{-6}$ mol·m^{-3}) for consistency.

²²² The subsequent bubbles were simulated subject to the same parameters, and protocol
²²³ described above. When the stop condition for the second bubble growth was reached (same
²²⁴ for the first bubble, i.e., $r_{min} \leq 20$ nm), the departure and rising event were then simulated
²²⁵ according to the procedure described in the previous paragraphs. This setup was consid-
²²⁶ ered for the seven cycles simulated herein. Figure 2 presents a flow chart summarizing the
²²⁷ procedure adopted in the numerical simulations.

²²⁸ Finally, the electrode inner radius R_{in} and electrode width R_w were changed and bubble
²²⁹ growth was simulated at i = 10 μA and i = 50 μAwith the same stop condition as above.
²³⁰ R_i and R_w were changed such that the area of the electrode in all cases was the same. This
²³¹ was done in order to maintain the same current density in all cases. Each case was preceded
²³² by a preliminary simulation with a stationary bubble to estimate the nucleation time and
²³³ determine the duration of the time-dependent concentration ramp at the bubble interface
²³⁴ as described above. In total, 5 cases were simulated and correspond to $R_e/R_d =$ 0.24, 0.51,
²³⁵ 0.66, 1.01 and 1.32 where $R_e = R_{in} + R_w/2$, is the mean electrode radius, and R_d is the
²³⁶ radius of the bubbles at departure. R_d was constant in all simulations reported in this study
²³⁷ because the pit radius R_p was not varied, and R_d is determined by the radius of the pinning
²³⁸ line. The exact values of R_{in}, and R_w are given in SI Sec. S1.2.

12

239 *2.1. Mathematical Model*

240 *2.1.1. Fluid Dynamics*

241 The bubble growth and bubble rising events were calculated with the moving mesh Ar-
242 bitrary Lagrangian–Eulerian (ALE) formulation [6, 12, 23].

243 The 2D axisymmetric, Newtonian, time-dependent, laminar and incompressible flow oc-
244 curring in the device was modeled according to the momentum and overall mass balance
245 equations represented by Eqs. 1 and 2, respectively:

$$\rho\frac{\partial \mathbf{u}}{\partial t} + \rho(\mathbf{u} \cdot \nabla)\mathbf{u} = \nabla \cdot [-p\mathbf{I} + \mu(\nabla\mathbf{u} + (\nabla\mathbf{u})^T)] + \rho\mathbf{g} \tag{1}$$

$$\nabla \cdot \mathbf{u} = 0 \tag{2}$$

246 where ρ (kg·m^{-3}) is the density, $\mathbf{u}$ (m·s^{-1}) is the velocity field, p (kg·m^{-1}·s^{-1}) is the pres-
247 sure, μ (kg·m^{-1}·s^{-1}) is the dynamic viscosity, $\mathbf{I}$ (dimensionless) is the identity matrix, T
248 (dimensionless) is the transpose operator and $\mathbf{g}$ (m·s^{-2}) is the gravity acceleration.

249 At the gas-liquid interface, the finite stresses were calculated according to Eq. 3.

$$\mathbf{n}_1 \cdot (\boldsymbol{\tau}_1 - \boldsymbol{\tau}_2) = \boldsymbol{f}_{st} \tag{3}$$

250 where $\boldsymbol{\tau}_1$ (N·m^{-2}) and $\boldsymbol{\tau}_2$ (N·m^{-2}) are the total stress tensors in each phase (gas and liquid,
251 respectively) at the interface ($\boldsymbol{\tau}_i = -p\boldsymbol{I} + \mu_i(\nabla\boldsymbol{u}_i + (\nabla\boldsymbol{u}_i)^T)$), while $\boldsymbol{n}$ (dimensionless) is the
252 normal to the interface. The term $\boldsymbol{f}_{st}$ (N·m^{-2}) corresponds to the force per unit area related
253 to the surface tension, expressed in Eq. 4.

$$\boldsymbol{f}_{st} = \sigma(\nabla_t \cdot \boldsymbol{n}_1)\boldsymbol{n}_1 - \nabla_t\sigma \tag{4}$$

254 where σ is the surface tension coefficient (N·m^{-1}) and ∇_t is the surface gradient operator.

255 Moreover, continuity of the velocity field is considered at the interface, according to Eq.

13

5.

$$\boldsymbol{u}_1 = \boldsymbol{u}_2 + M_f \left(\frac{1}{\rho_1} - \frac{1}{\rho_2} \right) \boldsymbol{n}_1 \tag{5}$$

where $\boldsymbol{u}_1$ (m·s^{-1}) and $\boldsymbol{u}_2$ (m·s^{-1}) are the velocity of the gas and liquid phases, respectively, at the interface.

M_f (kg·m^{-2}·s^{-1}) is the interfacial H$_2$ mass flux given by Eq. 6.

$$M_f = (J_{H_{2,r}} \cdot n_{1,r} + J_{H_{2,z}} \cdot n_{1,z}) MW_{H_2} \tag{6}$$

where $J_{H_{2,r}}$ and $J_{H_{2,z}}$ (kmol·m^{-2}·m^{-1}) are the diffusive flux of H$_2$ in the r and z directions, respectively, n_r and n_z are the r and z normal components at the gas-liquid interface, and MW_{H_2} (kg·kmol^{-1}) is the molecular weight of H$_2$.

Finally, the mesh velocity was calculated according to Eq. 7.

$$\boldsymbol{u}_{mesh} \cdot \boldsymbol{n}_1 = \left(\boldsymbol{u} - \frac{M_f}{\rho_1} \boldsymbol{n}_1 \right) \cdot \boldsymbol{n}_1 \tag{7}$$

No-slip conditions were considered at the walls. Moreover, null gauge pressure was applied at the top surface of the computational domain (open to the atmosphere).

2.1.2. Mass Transfer

The time-dependent convection-diffusion equation (Eq. 8) was used to model the transport of hydrogen in the liquid phase.

$$\frac{\partial c_{H_2}}{\partial t} + \nabla \cdot \boldsymbol{J}_{H_2} + \boldsymbol{u} \cdot \nabla c_{H_2} = 0 \tag{8}$$

where c_{H_2} (mol·m^{-3}) is the concentration of H$_2$ in the liquid phase, $\boldsymbol{J}_{H_2}$ (kmol·m^{-2}s^{-1}) is the diffusive flux of H$_2$ in the liquid phase and $\boldsymbol{u}$ (m·s^{-1}) is the velocity field.

The diffusive flux of H$_2$ in the liquid phase was modeled by Fick's first law, given by Eq. 9.

14

$$\boldsymbol{J}_{H_2} = -D\nabla c_{H_2} \tag{9}$$

273 where D (m^2·s^{-1}) is the H$_2$ diffusivity in the liquid phase.

274   H$_2$ impermeability (-$\boldsymbol{n}$·$\boldsymbol{J}_{H_2}$= 0) was considered at the walls. A specified H$_2$ flux was im-

275 posed at the ring electrode's surface (-$\boldsymbol{n}$·$\boldsymbol{J}_{H_2}$=$\boldsymbol{J}_{H_{2,0}}$). Moreover, the H$_2$ saturation concentra-

276 tion c_s =7.7×10^{-6} mol·m^{-3} was considered at the gas-liquid interface. Null H$_2$ concentration

277 was considered at the top of the computational domain.

3. Results and discussion

3.1. Bubble growth

280   The experimental curves, and the growth law applicable to bubble growth in this system

281 have been discussed in detail in a previous publication [43]. In brief, the bubbles growing at

282 the center of the ring electrode have been shown to transition from pressure-driven growth,

283 to diffusion-limited growth, and finally to reaction-limited (also referred to as supply-limited)

284 growth for $R_b > R_e$; where R_e is the mean electrode radius. In other words, the value of the

285 exponent α, the exponent in the bubble growth law $R_b = \beta t_b^{\alpha}$, decreases from 1 at the start

286 of electrolysis to 1/2 during the diffusion-limited phase, and to 1/3 when the bubble begins

287 to eclipse the electrode.

288   The results from the simulation were processed identically to the experimental results to

289 ensure comparability. A key limitation in our experimental setup is that, when imaged from

290 the top, bubbles smaller than the pit radius are indistinguishable from the pit itself. This

291 limitation is mimicked by our model where the radius of the simulated bubbles are taken

292 to be the maximum of the r-coordinate along the bubble interface at any given instance in

293 time. In practice, this means that, $R_b < 10$ μm are not simulated. Note that initially, the

294 bubble grows as a spherical cap of a sphere whose true geometric radius is much larger than

295 the pit radius. This spherical radius is not meaningful for the discussion presented here and

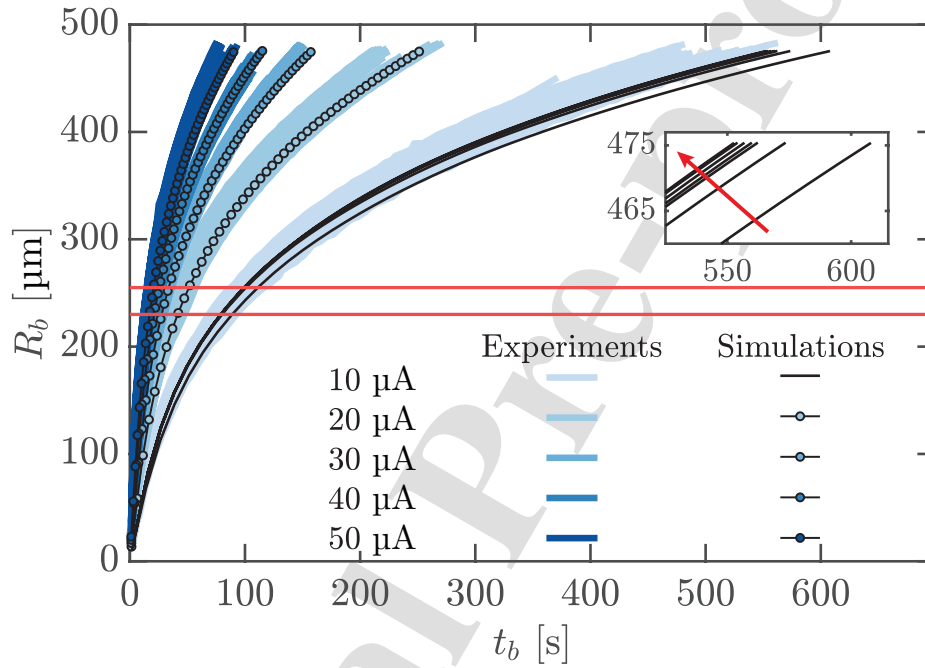296 was therefore not measured in either the experiment, or the models.

15

Figure 3: Bubble radius R_b of both experimental and simulated bubbles plotted against bubble lifetime t_b. The experimental curves from Raman et al. [43] (blue lines) represent data from 332 bubbles spread across 25 experiments driven by five currents (see legend). The growth curves of a single simulated bubble driven by the four higher currents (20 μA to 50 μA) are shown as circles connected by lines (note that the circles on the simulated curves are undersampled for better readability). The growth curves for 7 successive simulated bubbles driven by 10 μA are plotted as black lines. The inset shows the a zoom-in of growth curves of the seven bubbles driven by 10 μA just before departure. The growth curves for the second to seventh bubbles lie close to one another but are distinct from the first bubble. The horizontal red lines show the inner and outer diameters of the ring electrode. The direction of the red arrow in the inset indicates the succession of bubble growth curves.

297 Fig. 3 shows R_b from experiments and simulations plotted against the corresponding

298 bubble lifetimes, t_b for different constant applied currents, i. The bubble nucleation time t_0

299 for the first simulated bubbles was measured by calculating the linear extrapolation whereas,

300 the nucleation times of subsequent bubbles is known precisely. The bubble lifetime, t_b is then

301 calculated as $t - t_0$ where t is experimental, or simulated time. The experimental curves

302 depict the full spread of data, without distinction between successive bubbles from multiple

303 experiments [43].

304 Fig. 3 also shows that all simulated bubble growth curves lie within the spread of exper-

305 imental data. Nevertheless, the model under-predicts the growth rate of bubbles compared

306 to the mean (not plotted) of the experimental data spread from experimental observations.

307 The model predicts that the bubbles take 10-20 % longer to reach the departure radius than

308 the mean departure time from experiments. This is particularly visible for $t_b > 400$ s for the

309 first bubble driven by $i = 10$ μA.

310 To further investigate the source of this deviation, seven successive bubbles driven by an

311 electrolysis current of 10 μA were simulated.The second bubble reaches its departure radius

312 $\sim 6.2\%$ sooner than the first bubble. However, the inset in Fig. 3, shows that the initial

313 transience quickly approaches a steady-state, and the growth curves of successive bubbles

314 are almost identical. For instance, the departure times of the sixth, and the seventh bubbles

315 differ by $\sim 0.25\%$ (see SI Table SI 2 for bubble departure times). Therefore, it is reasonable

316 to attribute this transience to the development of a pseudo-steady concentration field around

317 the electrode. The development, and stabilization of the concentration field is discussed in

318 Sec. 3.4.

319 Similar start-up transients have been observed in a previous study of successive elec-

320 trolytic bubbles [58]. Bubbles in the earlier study grew on electrodes several times larger

321 than their departure radius i.e., $R_b \ll R_e$, with a much lower gas-evolution efficiency (see

322 Eq. 10) and took > 20 min to reach steady-state at current densities up to two orders of

323 magnitude smaller than those considered in this study. Our findings provide a contrasting
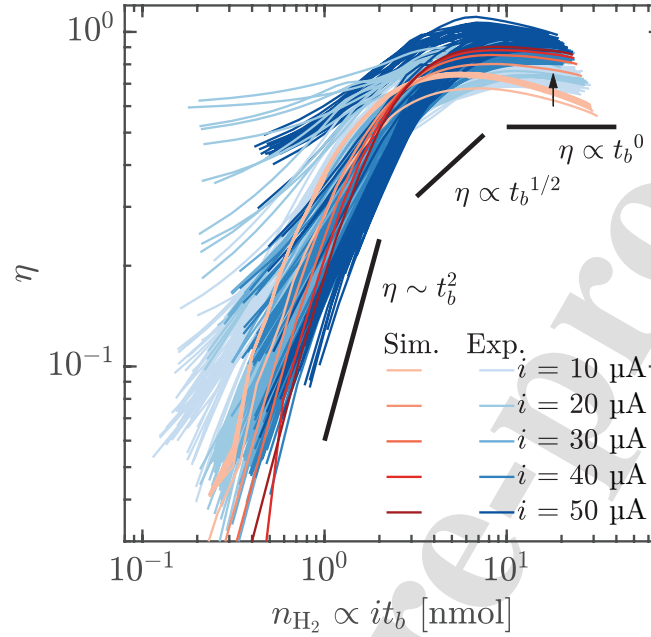
17

Figure 4: Comparison of experimental [43] and simulated instantaneous gas evolution efficiencies for different currents. Instantaneous gas evolution efficiency, η, plotted against the number of moles of hydrogen generated at the electrode at that instant, n_{H_2}. The black arrow indicates curves of the seven successive bubbles driven by 10 µA .

case where the number of bubble departures required to reach a pseudo-steady concentration field around the electrode is much smaller as a consequence of the bubbles growing to a maximum of $R_b/R_e \simeq 2$. The ring electrode system presented in this study is a closer representation of a unit cell with a single gas bubble on an electrode.

3.2. Instantaneous gas evolution efficiency

From Fig. 3 we learn that the simulated bubbles appear to grow slower than their experimental counterparts in the reaction-limited growth phase i.e., $R_b/R_e > 1$. We explore this further by considering the instantaneous gas evolution efficiency, η which is plotted against n_{H_2}, the number of moles of hydrogen generated at the electrode in Fig. 4. Here, η is defined as:

$$\eta = \frac{dn_b/dt_b}{dn_{H_2}/dt_b} = \frac{4\pi P_0/3\mathcal{R}T_0}{i/2F}\frac{dR_b^3}{dt_b} = \frac{J_b A_b}{i/2F} \tag{10}$$

18

334 where, P_0 is the ambient pressure, T_0 is the ambient temperature, $\mathcal{R}$ is the universal gas

335 constant, J_b is the molar flux of H_2 into the bubble, $A_b = 4\pi R_b^2$ is the area of the gas-liquid

336 interface, and F is the Faraday constant. Thus, η is ratio of the rate of uptake of gas by the

337 bubble and the Faradaic rate of generation of gas at the electrode surface . The instantaneous

338 gas evolution efficiency for experimental bubbles was calculated by fitting a smoothing spline

339 and then numerically calculating the derivative dR_b^3/dt_b [43]. Since it is possible to obtain

340 J_b directly from the simulations, the η for the simulated bubbles is directly calculated as the

341 ratio specified on the right hand side of Eq. 10.

342   The η of both experimental, and simulated bubbles increases with increasing current

343 density. The simulated bubbles also demonstrate the experimentally observed transition

344 from pressure-driven ($\eta \sim t_b^2$) to diffusion-limited ($\eta \sim t_b^{1/2}$), and finally to supply-limited

345 ($\eta \sim t_b^0$) growth. While there is a small decrease in the efficiency of experimental bubbles

346 for the reaction-limited (supply-limited) regime just before departure, η for the simulated

347 bubbles reaches a noticeable maximum before the bubble departure. This is more evident in

348 the case of bubbles driven by 10 μA $n_{H_2} > 4$ nmol or, $\sim t_b > 80$ s. This region of decreasing

349 η before departure coincides with the aforementioned slower bubble growth observed for

350 simulated bubbles in Fig. 3.

351   The spatial separation of the site of bubble nucleation from the site of electrolysis (the

352 electrode surface) has interesting implications for the time evolution of η, and the concen-

353 tration field around the bubble. Since the bubble does not grow directly on the electrode

354 surface, there is a finite diffusive flux of H_2 from the electrode towards the bulk electrolyte.

355 Thus, the bubble effectively experiences only a fraction of the total Faradaic flux out of the

356 surface of the electrode. The evolution of η seen in Fig. 4 describes the fraction of the flux

357 at the electrode which drives bubble growth at a given instant. This fraction is determined

358 by the geometry of the system at a given time, which is characterized by R_b/R_e. In the

359 diffusive-growth regime, R_b/R_e is a measure of the distance the gas has to diffuse before

360 reaching the gas-liquid interface. Initially, when the bubble is small and the diffusion path

19

361 length between the electrode and the bubble interface is large, η is very low. As the bubble

362 grows, this distance decreases; resulting in an increased η.

363 Once the threshold $R_b/R_e > 1$ is reached, and the bubble transitions to supply-limited

364 growth, the diffusion path length is small and does not appreciably vary further. Diffusion

365 is no longer the limiting factor, and the bubble is expected to grow at a constant volumetric

366 rate. However, as noted earlier, we observe that the η in fact reaches a maxima in this phase

367 of bubble growth. During the early stages of bubble growth when η is low, a majority of

368 the H_2 produced at the electrode diffuses into the electrolyte in the vicinity of the electrode.

369 The emergence of the maxima in η seen in Fig. 4 can be explained by the re-absorption of

370 some of the H_2 that previously diffused into the electrolyte.

371 Previous studies have shown that bubbles growing atop a carpet of microbubbles, grow

372 with 100 % gas evolution efficiency in a reaction-limited regime when $R_b > R_e$ [70]. In

373 contrast, bubbles in our system exhibit $\eta < 1$ despite growing at a constant volumetric

374 rate indicating that the bubble does not capture all of the H_2 produced at the electrode

375 surface. We explore the reasons for this in Sec. 3.3 by considering the concentration profile

376 of dissolved hydrogen in the vicinity of the bubble.

377 *3.3. Flux along the bubble surface*

378 The spatio-temporal evolution of the flux of H_2 along the bubble surface was evaluated

379 using the model, and Fig. 5 shows the Lagrangian multiplier of the concentration of H_2, c_{lm},

380 which represents the line integral of the flux of H_2 along the circumference of the bubble sur-

381 face at a given height. This integral is normalized by the Faradaic flux, and plotted against

382 the non-dimensionalized bubble height z/z_{max}, at different non-dimensionalized bubble life-

383 times t_b/t_d. Here, z_{max} is the height of the bubble at a given time, and t_d is the time at

384 which the bubble departs from the pit. From Fig. 5, we make four key observations that

385 shed further light on the evolution of η discussed in Sec. 3.2.

386 Firstly, the total molar rate of transport of H_2 into the bubble, which is the area under

387 the curves in Fig. 5, increases with time. This agrees well with transition of the bubble from
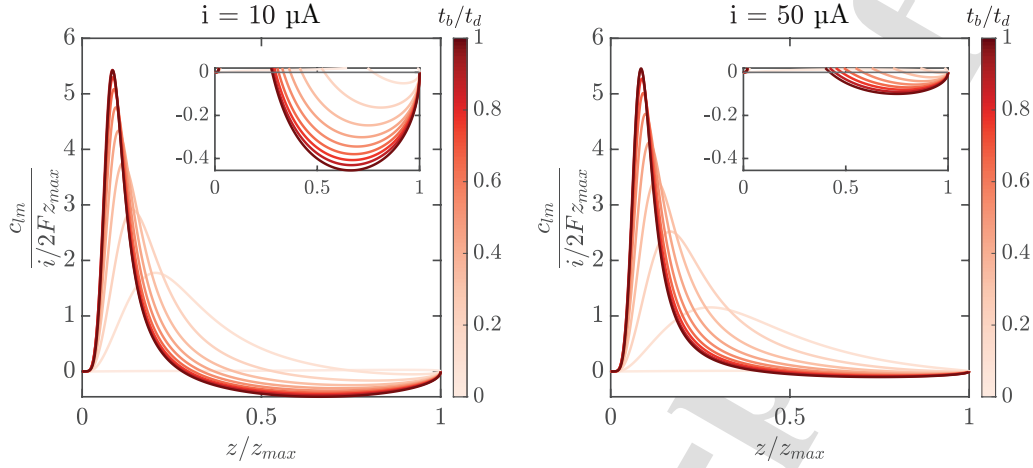
20

Figure 5: The flux at points along the bubble interface is normalized by the Faradaic flux at the electrode $i/2FA_e$ and plotted as a function of fractional height z_i/z_{max} at different normalized times t_b/t_d (see colorbar) at the lowest (left panel, 10 μA), and the highest (right panel, 50 μA) currents considered in the study. c_{lm} is the Lagrangian multiplier of concentration, and represents the line integral of flux along the surface of the bubble at a given height. Therefore, the quantity $c_{lm}/(i/2Fz_{max})$ is calculated as a function of the height along the bubble interface. The x-axis extends from the bottom of the bubble where it is pinned to the pit ($z/z_{max} = 0$) to the apex of the bubble ($z/z_{max} = 1$). The zoom-ins (insets) show that flux turns negative across a section of the bubble's surface.
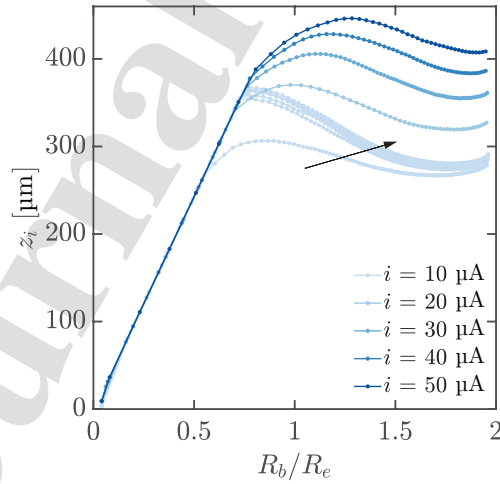
Figure 6: The variation of the flux inversion height i.e., the height along the bubble surface at which the gas diffuses from the bubble to the liquid, is plotted as a function of the non-dimensionalized bubble radius R_b/R_e. The direction of the arrow indicates the order of curves associated with successive bubbles driven by 10 μA from first to seventh.

21

the diffusion-limited regime to the supply-limited growth regime (discussed in Sec. 3.1 and Sec. 3.3).

Secondly, a peak in the flux curves increases in magnitude, and shifts towards the base of the bubble as it grows larger, and transitions to supply-limited growth. This indicates that the bulk of the flux into the bubble is concentrated near the base of the bubble close to the electrode surface. This has been previously reported as direct-injection, and is characteristic of supply-limited bubble growth [9, 42, 70].

Thirdly, there is a simultaneous outward diffusive flux of hydrogen from the apex of the bubble even as the bubble absorbs hydrogen at the bottom. The outward diffusive flux is visible as the negative portion of the curves in Fig. 5. The magnitude of this outward flux increases with increasing bubble radius. The portion of the bubble's total interfacial area from which hydrogen escapes into the electrolyte also increases with increasing R_b. The re-dissolution of hydrogen from the top of the bubble, contributes to the slight decline in η seen in Fig. 4, just before bubble departure.

Finally, the magnitude of the H_2 outward flux decreases with increasing i. This explains why the η curves of bubbles driven by an electrolysis current of 10 μA in Fig. 4 show a prominent maxima. This also explains why bubbles driven by higher currents are more efficient at gas uptake.

Fig. 6 shows the flux inversion height z_i as a function of the non-dimensionalized bubble radius R_b/R_e for different currents. We define z_i as the height along the bubble surface where the direction of the flux of hydrogen changes sign, or equivalent to the height of the bubble if no inversion happens. Initially, z_i varies linearly with R_b/R_e, and is $\sim R_b$. This indicates that the bubble is fully immersed in a region of the electrolyte which is saturated with hydrogen gas. Moreover, we note that apex hydrogen loss begins at a greater bubble radius, and at a greater height for higher currents. This happens because, higher electrolysis currents saturate the electrolyte in the vicinity of the bubble, faster. Additionally, successive bubbles driven by 10 μA also show hydrogen re-dissolution at greater heights, and radii. This

22

⁴¹⁵ is because the departure of previous bubbles induces a convective wake which saturates the

⁴¹⁶ electrolyte directly above the incipient bubble. Finally, the onset of apex hydrogen re-

⁴¹⁷ dissolution coincides with the transition to reaction-limited growth - both of which begin

⁴¹⁸ around $R_b = R_e$.
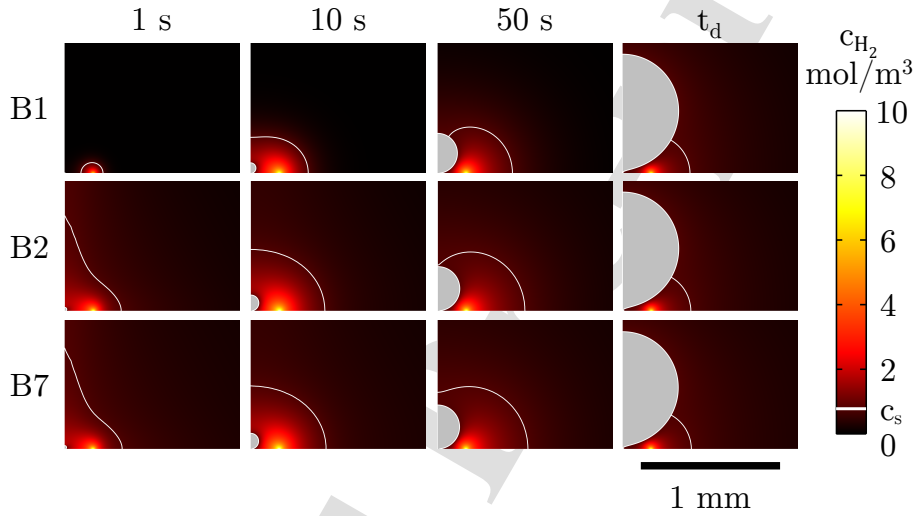
⁴¹⁹ *3.4. Evolution of concentration profiles*

Figure 7: The development of the concentration of dissolved hydrogen (see common colorbar) around successive electrolytic bubbles driven by a current of 10 μA is shown at different times - 1 s, 10 s, 50 s, and at t_d when the bubble reaches its departure radius. There is a marked difference between the concentration fields surrounding the first, and the second bubbles (rows B_1 and B_2, respectively). These differences are less remarkable between the second, and the seventh successive bubble (rows B_2 and B_7). Each panel has a white contour line representing the saturation boundary where $c_{H_2} = c_s$. Furthermore, the concentration field surrounding all three bubbles at t_d is similar.

⁴²⁰ Figure 7 shows the evolution of the concentration of dissolved hydrogen around a bubble

⁴²¹ driven by an electrolysis current of 10 μA. The concentration of dissolved hydrogen in the

⁴²² electrolyte near the electrode increases at the start of electrolysis. Thereafter, a diffusive

⁴²³ front is formed which grows until it reaches the superhydrophobic cavity at the center of

⁴²⁴ the ring electrode. In the absence of bubble nucleation, this diffusive front will continue to

⁴²⁵ expand. However, the nucleation of the bubble consumes dissolved gas from the supersat-

⁴²⁶ urated electrolyte. At its maximum extent, the saturated region extends up to ≈ 350 μm

23

from the substrate; beyond which the electrolyte remains undersaturated throughout the lifetime of the bubble. Initially, the bubbles are fully contained within the saturated region (indicated by white contours in Fig. 7) and therefore, after a short pressure-driven growth regime, exhibit diffusion-limited growth. As the bubble grows by diffusively absorbing hydrogen from the surrounding electrolyte, the bubble interface advances faster than the layer of saturated electrolyte. As a result, the top portion of the bubble is exposed to undersaturated electrolyte and the hydrogen in the bubble begins to re-dissolve at the bubble's apex.

Three important observations can be made from Fig. 7 when comparing different panels. Firstly, the concentration profile of dissolved hydrogen surrounding each bubble changes during its lifetime. This happens both for the first bubble, as well as the succeeding ones. This can be seen when comparing the concentration profiles for the same bubble at different times (along each row). Following the departure of the first bubble, the differences in the concentration profiles surrounding successive bubbles, compared at the same bubble lifetime, is minimal. This can be seen when comparing the concentration profiles of the second, and the seventh bubble at identical times in Fig. 7 (rows 2 and 3, along columns). Finally, the concentration profiles of the same bubble (same row in Fig. 7) does not change appreciably between 50 s and just before bubble departure (two right-most panels). The panels at $t_b = 50$ s were plotted because at t = 50 s, for bubbles driven by an electrolysis current of 10 µA, $R_b \simeq R_e$. This marks the transition from diffusion-limited growth to supply-limited (or reaction-limited) growth. Thus, temporal changes in the concentration profile occur mainly during diffusion-limited growth of the bubble.

Fig. 8 shows the departure of the first bubble generates a wake which disrupts the saturated region, and drags it upwards as the bubble rises. This can also be seen in Fig. 7 in the panels corresponding to 1 s after the nucleation of the third and seventh bubbles where the saturation contours extend upwards (left-most panels on rows B3 and B7). Departure-induced advection leads to the development of a pseudo-steady concentration profile. Successive bubbles remain within the elongated saturated region for a greater duration,

24

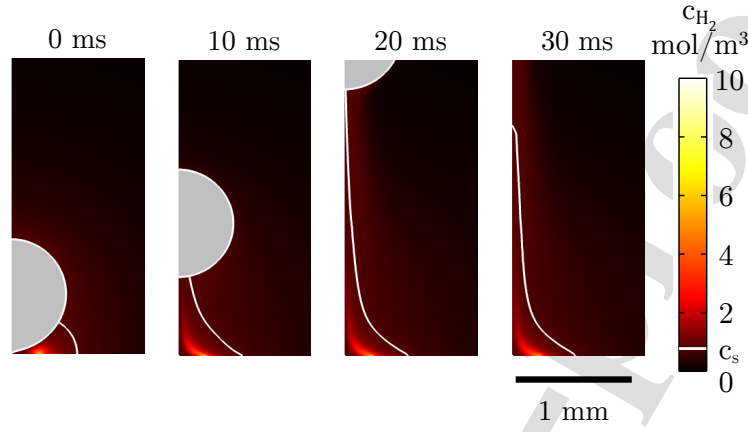Figure 8: The departure and rise of the first bubble driven driven by 10 μA is shown at 10 ms intervals after bubble departure. The generation of an advective wake, and the subsequent disruption of the concentration profile is visible. The white contour line denotes the extent of the saturation boundary where $c_{H_2} = c_s$.
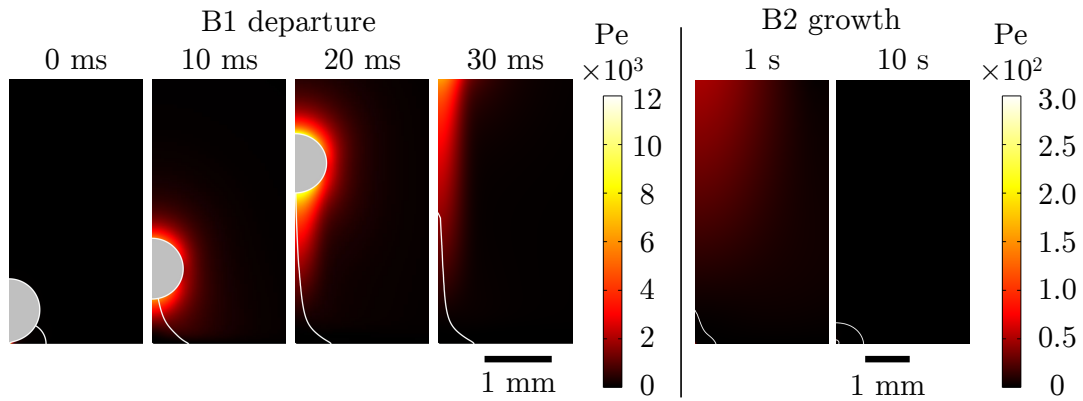

Figure 9: The local Peclet numbers, $Pe = R_e U / D$ are shown at 10 ms intervals after the departure for the first bubble driven by 10 μA. Similarly, the local Peclet numbers of second bubble are shown at $t_b = 1s$ and $t_b = 10s$. The white contour line denotes the extent of the saturation boundary where $c_{H_2} = c_s$. The plots show that advection caused by bubble departure strongly dominates the diffusive transport of hydrogen for a short duration (< 10 s) during, and after the departure of the preceding bubble.

454 and thus exhibit faster growth (see inset Fig. 3), and greater η (see Fig. 4). As noted above,

455 the concentration field surrounding all the bubbles just before departure is almost identical.

456 This indicates that the influence of the departure of the preceding bubble on the growth

457 of the subsequent one is limited to the elongation of the saturation boundary in the initial

458 stages of growth $R_b/R_e < 1$. The temporal limit of the influence of convection is also seen

459 in Fig. 9 where the Peclet number $Pe = R_e U/D$ is plotted; where U is the magnitude of

460 the electrolyte velocity, and D is the diffusivity of hydrogen in the electrolyte. Pe increases

461 around the bubble, and in its wake as it rises through the electrolyte upon departure. The

462 remnants of the wake are visible during the early stage of the growth of the subsequent

463 bubble but dissipates within 10 s.

4. Effect of ring electrode size

465 The diffusion path length for dissolved hydrogen in this system is the mean distance

466 from the surface of the electrode to the surface of the bubble. Therefore, the mean electrode

467 radius R_e has a profound impact on the growth dynamics of bubbles. As mentioned in Sec.

468 2, bubbles driven by an electrolysis current of 10 μA and 50 μA were studied for five different

469 mean electrode radii. The results discussed in previous sections correspond to a normalized

470 mean electrode radius $R_e/R_b = 0.51$.

471 Fig. 10 shows the evolution of bubble radius R_b for different R_e/R_d where R_d is the radius

472 of the bubble at departure. It is clear from Figs. 10(a) and 10(b) that bubbles growing at

473 the center of larger ring electrodes grow slower. As previously mentioned in Sec. 2, electrode

474 areas for all cases were kept constant. Therefore, despite being driven by the same current

475 density, bubbles grow slower as the electrode radius increases. This can be explained by the

476 increased diffusion path length for the dissolve hydrogen. The slower growth for the same

477 current also indicates that the overall gas evolution efficiency η decreases with increasing

478 R_e/R_d. This can also be seen in Fig. 11 where panels corresponding to larger R_e/R_d display

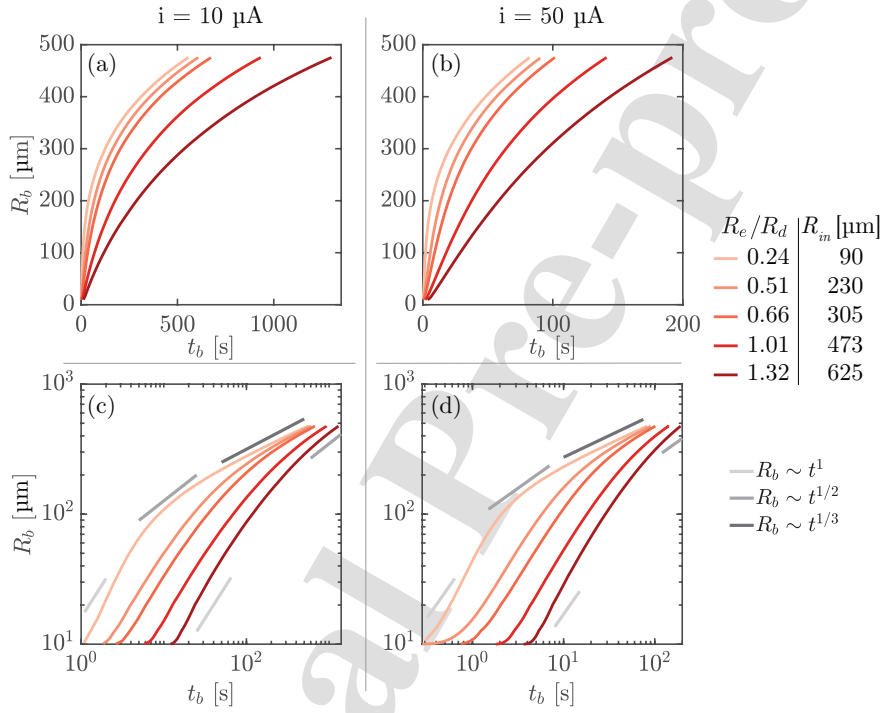479 a greater spread of dissolved hydrogen around the bubble.

26

Figure 10: The radius R_b of bubbles driven by two electrolysis currents (a,c) i = 10 μA and (b,d) i = 50 μA, growing at the center of ring electrodes of varying mean electrode radii, R_e are plotted as a function of bubble lifetime t_b. The growth curves are shown in both (a,b) a linear scale, as well as a (c,d) a logarithmic scale. In plots (c,d), the slopes corresponding to the pressure-driven ($R_b \sim t_b$), the diffusion-limited ($R_b \sim t_b^{1/2}$), and the supply-limited ($R_b \sim t_b^{1/3}$) growth regimes are indicated by the grey lines. The mean electrode radii are normalized by the departure radius R_d. Therefore, R_e/R_d is a measure of how large the electrode is in relation to the maximum size attained by the bubbles. The legends are common to all four plots.

27
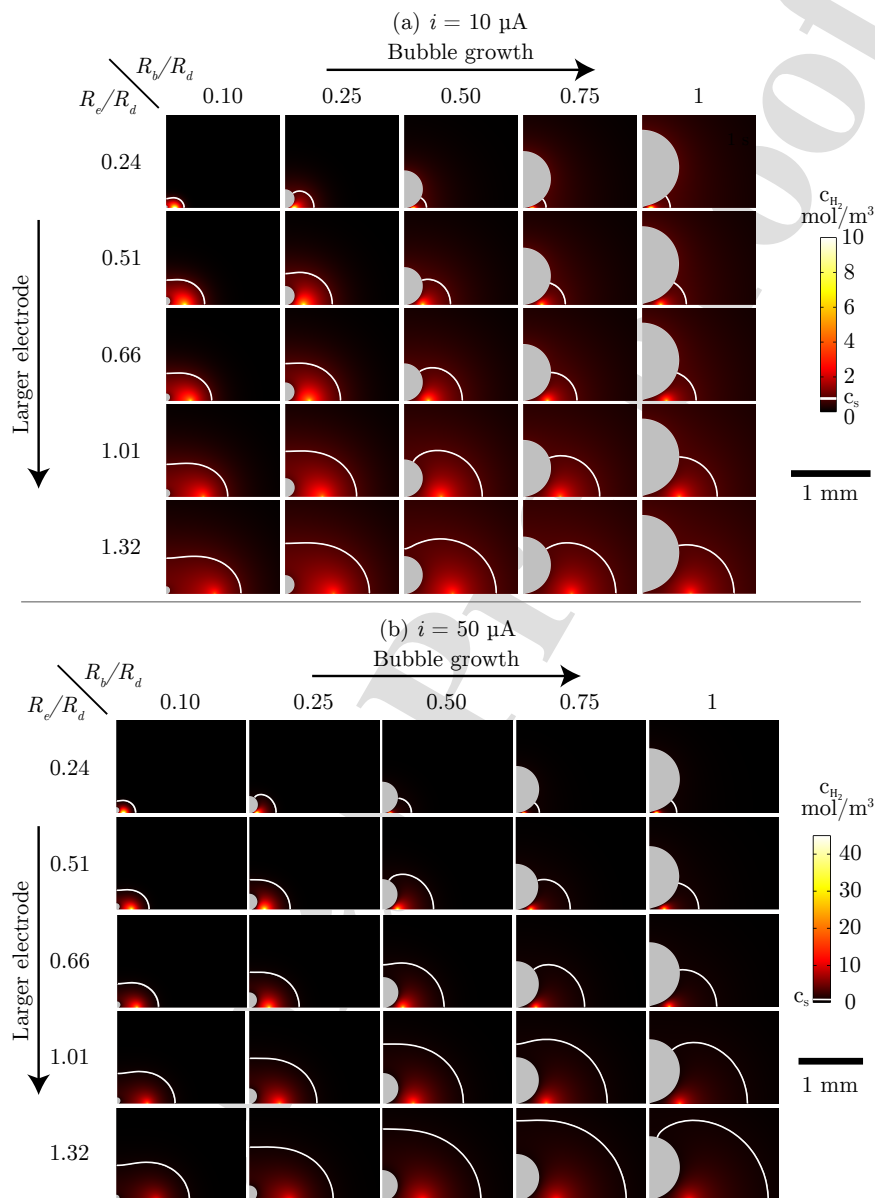
Figure 11: The temporal development of the concentration of dissolved hydrogen around bubbles growing at the center of ring electrodes of different mean electrode radii, are showing at different stages of growth for two currents - (a) 10 μA and (b) 50 μA. Snapshots of bubbles for each normalized mean electrode radius, R_e/R_d are selected at the five stages indicated by the normalized bubble radii R_b/R_d. Each panel has a white contour line representing the saturation boundary where $c_{H_2} = c_s$.

The position of the ring relative to the bubble radius at any given time, determines the gas evolution efficiency - the closer the bubble interface is to the electrode surface, the more efficient it is at gas uptake. As the bubble grows, the diffusion path length between the bubble interface and the electrode decreases and η increases as seen in Fig. 4. Gradually, the diffusion path length becomes so small that the growth of the bubble is only limited by the supply of dissolved gas from the electrode. This is when η plateaus (and then begins to drop due to re-dissolution at the apex).

The transition between the three bubble growth regimes is visible in Figs. 10(c) and 10(d) where the same bubble growth curves are shown on a logarithmic scale. On a logarithmic scale, the general bubble growth equation $R_b = \beta t_b^\alpha$ becomes $\log(R_b) = \log(\beta) + \alpha \log(t_b)$; where α and β is the growth . Hence, the nature of bubble growth can be estimated from the slope of the growth curve, α in a log-log plot The pressure-driven, diffusion-limited and supply-limited growth regimes correspond to slopes of 1, 1/2, and 1/3 respectively. It can be seen from 10(c,d) that bubbles surrounded by electrodes with electrode radii $R_e > R_d$ never enter the supply-limited phase, and grow entirely within the diffusion-limited regime. In such cases where the bubble departs in the diffusion-limited regime, it is likely that the number of bubble departures required to reach a pseudo-steady state will be much longer than the case seen in the inset in Fig. 3.

Since the growth rate of bubbles depends on R_e, the concentration profiles in Fig. 11 are compared at the same bubble radii relative to the departure radius R_d. It can be seen that flux inversion and the re-dissolution of hydrogen from the apex of the bubbles occurs for all R_e/R_d i.e., bubble outgrew the region of electrolyte saturated with hydrogen for all cases considered in this study. Further, this inversion occurs at a smaller R_b for smaller R_e. Note that the colorbars for panels corresponding to the two electrolysis currents in Fig. 11 are not the same. As the current increases, the size of the saturated layer increases, and the bubble radius at which re-dissolution commences also increases.

29

5. Conclusions and outlook

We have simulated the growth, and departure of electrolytic bubbles at different currents using a DNS approach. Our study considered the growth, and departure of successive electrolytic bubbles in a spatially decoupled system where the bubbles nucleation on a super-hydrophobic pit at the center of a ring electrode where the gas is generated. Moreover, the study considers larger bubbles than previously reported in the literature. These bubbles are shown to outgrow the concentration boundary layer which partly explains the rich bubble growth dynamics. A time-dependent investigation considering coupled fluid flow and mass transfer is presented, which represents a significant advancement regarding the study of Peñas et al. [41]. Finally, the use of an ALE moving mesh topology for the electrolytic bubbles and the use of an interface cutting protocol to handle topology changes during bubble departure are enable the precise calculation of gas flux along the bubble interface.

The simulated bubble growth curves show good agreement with experimental data. The bubbles transition from pressure-driven, to diffusion-limited, to reaction-limited growth. It was observed that the model predicted slower growth for the first bubble driven by the lowest current (10 μA) than seen in experiments. In order to further understand the reason for this, seven successive bubble growth and departures driven by 10 μA were simulated. It was observed that the time evolution of bubble radii of successive bubbles fell within the spread of experimental data indicating the presence of a start-up transience. The convection induced by the departure of successive bubbles was shown to aid the development of a pseudo-steady concentration profile, and the attenuation of the start-up transience.

Three key observations are made in both the experiments, and the model. First, the bubbles exhibit reaction-limited growth with $\eta < 1$, where η is the instantaneous gas evolution efficiency. Second, η reaches a maxima, and decreases in the reaction-limited regime, just before bubble departure. Third, the η of bubbles in the reaction-limited regime increases with increasing current. The underlying reasons for these three observations were explored through the simulations which provided access to spatio-temporal information about the flux

533 of H_2, and the concentration field around the bubble. These data, which are challenging to
534 measure in-situ, show that the three aforementioned observations are caused by the combi-
535 nation of: (i) the separation of the site of nucleation site from the site of electrolysis, and
536 (ii) the diffusive flux of H_2 from the apex of the bubble into the electrolyte.

537 These two effects appear more pronounced in the model than in the experiments. Fur-
538 thermore, no appreciable start-up transience was visible in the experiments even at the
539 lowest current. One plausible explanation is that the electrolyte may not have been entirely
540 quiescent during experiments. Relatively weak flows in the electrolyte could alter the con-
541 centration field around the bubble. For instance, taking a diffusion length scale equivalent
542 to the mean electrode radius $R_e = 242.5$ μm, a flow velocity > 20 μm/s would imply that
543 the Peclet number $Pe > 1$, and that advection is the dominant phenomena.

544 The extent of the saturated region provides a natural limit for the departure size of
545 electrolytic bubbles with optimal gas uptake characteristics i.e., high η. We have shown that
546 bubbles that outgrow the saturated region, exhibit a gas evolution efficiency $\eta < 1$ despite
547 growing in a reaction-limited regime. In other words, bubbles that outgrow the saturation
548 region are less efficient at removing dissolved hydrogen from the vicinity of the electrode.
549 The ability of electrolytic bubbles to act as sinks for dissolved gas generated at the electrode
550 is fundamental to their concentration lowering effect which is the positive effect bubbles
551 have on electrolysis. Therefore, the extent of the saturated electrolyte provides the limit
552 for optimal bubble departure radius. Bubbles driven by smaller ring electrodes and greater
553 electrolysis currents are expected to be most efficient if they depart before outgrowing the
554 extent of the saturated electrolyte.

555 Forced convection of the electrolyte over the electrode is expected to change the size of
556 the saturated zone significantly. Furthermore, the region of saturated electrolyte surrounding
557 several bubbles growing in close proximity are expected to overlap - leading to more intricate
558 mass transfer dynamics. This scenario is further complicated by bubble coalescence which
559 will disrupt the concentration field. Further studies focusing on these effects are required to

31

560 fully understand, and optimize the gas evolution efficiency of electrolytic bubbles.

Declaration of Competing Interests

562 The authors declare that they have no known competing financial interests or personal
563 relationships that could have appeared to influence the work reported in this paper.

Credit authorship contribution statement

565 A.R., Conceptualization, Data Curation, Formal Analysis, Investigation, Methodology, Project
566 administration, Software, Visualization, Writing – original draft, Writing – review & editing.
567 C.C.d.S.P, Software, Writing – review & editing.
568 H.G., Funding acquisition, Project administration, Supervision, Writing – review & editing.
569 C.S., Funding acquisition, Methodology, Software, Writing – review & editing.
570 D.F.R., Funding acquisition, Project administration, Resources, Supervision, Writing – re-
571 view & editing.
572 N.P., Funding acquisition, Investigation, Methodology, Software, Validation, Writing – orig-
573 inal draft, Writing – review & editing.

Acknowledgements

Supplementary information

Supplemental information can be found in online version, at dx.doi.org/xx.xxx.xxxx.

References

[1] Alamri, B.R., Alamri, A.R.: Technical review of energy storage technologies when integrated with intermittent renewable energy. In: 2009 Int. Conf. Sustain. Power Gener. Supply, pp. 1–5 (2009). DOI 10.1109/SUPERGEN.2009.5348055

[2] Amestoy, P.R., Duff, I.S., L'Excellent, J.Y., Koster, J.: A Fully Asynchronous Multifrontal Solver Using Distributed Dynamic Scheduling. SIAM J. Matrix Anal. Appl. **23**(1), 15–41 (2001). DOI 10.1137/S0895479899358194

[3] Amestoy, P.R., Guermouche, A., L'Excellent, J.Y., Pralet, S.: Hybrid scheduling for the parallel solution of linear systems. Parallel Computing **32**(2), 136–156 (2006). DOI 10.1016/j.parco.2005.07.004

[4] Angulo, A., van der Linde, P., Gardeniers, H., Modestino, M., Fernández Rivas, D.: Influence of Bubbles on the Energy Conversion Efficiency of Electrochemical Reactors. Joule **4**(3), 555–579 (2020). DOI 10.1016/j.joule.2020.01.005

[5] Angulo, A.E., Frey, D., Modestino, M.A.: Understanding Bubble-Induced Overpotential Losses in Multiphase Flow Electrochemical Reactors. Energy Fuels (2022). DOI 10. 1021/acs.energyfuels.2c01543

[6] Anjos, G., Mangiavacchi, N., Borhani, N., Thome, J.R.: 3D ALE Finite-Element Method for Two-Phase Flows With Phase Change. Heat Transf. Eng. **35**(5), 537–547 (2014). DOI 10.1080/01457632.2013.833407

[7] Ascher, U.M., Petzold, L.R.: Computer Methods for Ordinary Differential Equations and Differential-Algebraic Equations. SIAM (1998)

[8] Bleeker, J., Kahn, A.P., Baumgartner, L.M., Grozema, F.C., Vermaas, D.A., Jager, W.F.: Quinolinium-Based Fluorescent Probes for Dynamic pH Monitoring in Aqueous Media at High pH Using Fluorescence Lifetime Imaging. ACS Sens. (2023). DOI 10.1021/acssensors.3c00316

[9] Brandon, N.P., Kelsall, G.H.: Growth kinetics of bubbles electrogenerated at microelectrodes. J Appl Electrochem **15**(4), 475–484 (1985). DOI 10.1007/BF01059288

[10] Catañeda, L.F., Rivera, F.F., Pérez, T., Nava, J.L.: Mathematical modeling and simulation of the reaction environment in electrochemical reactors. Current Opinion in Electrochemistry **16**, 75–82 (2019). DOI 10.1016/j.coelec.2019.04.025

[11] Chen, J., Guo, L., Hu, X., Cao, Z., Wang, Y.: Dynamics of single bubble departure from TiO2 nanorod-array photoelectrode. Electrochimica Acta **274**, 57–66 (2018). DOI 10.1016/j.electacta.2018.04.051

[12] Donea, J., Huerta, A., Ponthot, J.P., Rodríguez-Ferran, A.: Arbitrary Lagrangian–Eulerian Methods. In: Encyclopedia of Computational Mechanics, chap. 14, pp. 414–437. John Wiley & Sons, Ltd (2004). DOI 10.1002/0470091355.ecm009

[13] Dukovic, J., Tobias, Charles: The Influence of Attached Bubbles on Potential Drop and Current Distribution at Gas-Evolving Electrodes. J. Electrochem. Soc. **134**(2), 331 (1987). DOI 10.1149/1.2100456

[14] El-Askary, W.A., Sakr, I.M., Ibrahim, K.A., Balabel, A.: Hydrodynamics characteristics of hydrogen evolution process through electrolysis: Numerical and experimental studies. Energy **90**, 722–737 (2015). DOI 10.1016/j.energy.2015.07.108

[15] Gabrielli, C., Huet, F., Keddam, M., Rousseau, P., Vivier, V.: Scanning Electrochemical Microscopy for Investigating Gas Bubble/Liquid Interfaces. Electrochem. Solid-State Lett. **6**(10), E23 (2003). DOI 10.1149/1.1604971

[16] German, S.R., Edwards, M.A., Ren, H., White, H.S.: Critical Nuclei Size, Rate, and Activation Energy of H2 Gas Nucleation. J. Am. Chem. Soc. **140**(11), 4047–4053 (2018). DOI 10.1021/jacs.7b13457

[17] Grombik, I., Lasa, J., Šliwka, I., Mochalski, P., Pusz, J., Jackowicz-Korczynski, M.: New method of measuring hydrogen concentration in air. Environ. Prot. Eng. (2006)

[18] Gueyffier, D., Li, J., Nadim, A., Scardovelli, R., Zaleski, S.: Volume-of-Fluid Interface Tracking with Smoothed Surface Stress Methods for Three-Dimensional Flows. Journal of Computational Physics **152**(2), 423–456 (1999). DOI 10.1006/jcph.1998.6168

[19] Hreiz, R., Abdelouahed, L., Fünfschilling, D., Lapicque, F.: Electrogenerated bubbles induced convection in narrow vertical cells: PIV measurements and Euler–Lagrange CFD simulation. Chemical Engineering Science **134**, 138–152 (2015). DOI 10.1016/j.ces.2015.04.041

[20] International Energy Agency: The Future of Hydrogen. Tech. rep., IEA, IEA, Paris (2021)

[21] International Energy Agency: Net Zero by 2050. Tech. rep., IEA, IEA, Paris (2021)

34

[22] Iwata, R., Zhang, L., Wilke, K.L., Gong, S., He, M., Gallant, B.M., Wang, E.N.: Bubble growth and departure modes on wettable/non-wettable porous foams in alkaline water splitting. Joule **5**(4), 887–900 (2021). DOI 10.1016/j.joule.2021.02.015

[23] Jafari, R., Okutucu-Özyurt, T.: 3D numerical modeling of boiling in a microchannel by arbitrary Lagrangian–Eulerian (ALE) method. Applied Mathematics and Computation **272**, 593–603 (2016). DOI 10.1016/j.amc.2015.03.042

[24] Khalighi, F., Deen, N.G., Tang, Y., Vreman, A.W.: Hydrogen bubble growth in alkaline water electrolysis: An immersed boundary simulation study. Chemical Engineering Science **267**, 118280 (2023). DOI 10.1016/j.ces.2022.118280

[25] Lee, J.K., Bazylak, A.: Bubbles: The Good, the Bad, and the Ugly. Joule **5**(1), 19–21 (2021). DOI 10.1016/j.joule.2020.12.024

[26] Leenheer, A.J., Atwater, H.A.: Imaging Water-Splitting Electrocatalysts with pH-Sensing Confocal Fluorescence Microscopy. J. Electrochem. Soc. **159**(9), H752–H757 (2012). DOI 1

[27] Leistra, J.A.: Voltage Components at Gas Evolving Electrodes. J. Electrochem. Soc. **134**(10), 2442 (1987). DOI 10.1149/1.2100218

[28] Leistra, J.A., Sides, P.J.: Hyperpolarization at gas evolving electrodes—II. Hall/heroult electrolysis. Electrochimica Acta **33**(12), 1761–1766 (1988). DOI 10.1016/0013-4686(88) 85011-4

[29] Li, J., Gong, S., Zhang, L., Cheng, P., Ma, X., Hong, F.: Wetting States and Departure Diameters of Bubbles on Micro-/Nanostructured Surfaces. Langmuir **38**(10), 3180–3188 (2022). DOI 10.1021/acs.langmuir.1c03212

[30] Liu, H., Pan, L.m., Wen, J.: Numerical simulation of hydrogen bubble growth at an electrode surface. Can. J. Chem. Eng. **94**(1), 192–199 (2016). DOI 10.1002/cjce.22378

[31] Liu, Y., Jin, C., Liu, Y., Ruiz, K.H., Ren, H., Fan, Y., White, H.S., Chen, Q.: Visualization and Quantification of Electrochemical H2 Bubble Nucleation at Pt, Au, and MoS2 Substrates. ACS Sens. **6**(2), 355–363 (2021). DOI 10.1021/acssensors.0c00913

[32] Liu, Y., Lu, X., Peng, Y., Chen, Q.: Electrochemical Visualization of Gas Bubbles on Superaerophobic Electrodes Using Scanning Electrochemical Cell Microscopy. Anal. Chem. **93**(36), 12337–12345 (2021). DOI 10.1021/acs.analchem.1c02099

[33] Lohse, D.: Bubble puzzles: From fundamentals to applications. Phys. Rev. Fluids **3**(11), 110504 (2018). DOI 10.1103/PhysRevFluids.3.110504

[34] Lörstad, D., Fuchs, L.: High-order surface tension VOF-model for 3D bubble flows with high density ratio. Journal of Computational Physics **200**(1), 153–176 (2004). DOI 10.1016/j.jcp.2004.04.001

[35] Lv, P., Peñas, P., Le The, H., Eijkel, J., van den Berg, A., Zhang, X., Lohse, D.: Self-Propelled Detachment upon Coalescence of Surface Bubbles. Phys. Rev. Lett. **127**(23), 235501 (2021). DOI 10.1103/PhysRevLett.127.235501

[36] Massing, J., Mutschke, G., Baczyzmalski, D., Hossain, S.S., Yang, X., Eckert, K., Cierpka, C.: Thermocapillary convection during hydrogen evolution at microelectrodes. Electrochimica Acta **297**, 929–940 (2019). DOI 10.1016/j.electacta.2018.11.187

[37] Meulenbroek, A.M., Vreman, A.W., Deen, N.G.: Competing Marangoni effects form a stagnant cap on the interface of a hydrogen bubble attached to a microelectrode. Electrochimica Acta **385**, 138298 (2021). DOI 10.1016/j.electacta.2021.138298

[38] Moriarty, P., Honnery, D.: Intermittent renewable energy: The only future source of hydrogen? International Journal of Hydrogen Energy **32**(12), 1616–1624 (2007). DOI 10.1016/j.ijhydene.2006.12.008

[39] Pande, N., Chandrasekar, S.K., Lohse, D., Mul, G., Wood, J.A., Mei, B.T., Krug, D.: Electrochemically Induced pH Change: Time-Resolved Confocal Fluorescence Microscopy Measurements and Comparison with Numerical Model. J. Phys. Chem. Lett. **11**(17), 7042–7048 (2020). DOI 10.1021/acs.jpclett.0c01575

[40] Pande, N., Mul, G., Lohse, D., Mei, B.: Correlating the Short-Time Current Response of a Hydrogen Evolving Nickel Electrode to Bubble Growth. J. Electrochem. Soc. **166**(10), E280–E285 (2019). DOI 10.1149/2.0191910jes

[41] Peñas, P., van der Linde, P., Vijselaar, W., van der Meer, D., Lohse, D., Huskens, J., Gardeniers, H., Modestino, M.A., Rivas, D.F.: Decoupling Gas Evolution from Water-Splitting Electrodes. J. Electrochem. Soc. **166**(15), H769–H776 (2019). DOI 10.1149/2.1381914jes

[42] Qin, J., Xie, T., Zhou, D., Luo, L., Zhang, Z., Shang, Z., Li, J., Mohapatra, L., Yu, J., Xu, H., Sun, X.: Kinetic study of electrochemically produced hydrogen bubbles on Pt electrodes with tailored geometries. Nano Res. (2021). DOI 10.1007/s12274-020-3132-y

[43] Raman, A., Peñas, P., van der Meer, D., Lohse, D., Gardeniers, H., Fernández Rivas, D.: Potential response of single successive constant-current-driven electrolytic hydrogen bubbles spatially separated from the electrode. Electrochimica Acta **425**, 140691 (2022). DOI 10.1016/j.electacta.2022.140691

[44] Rivera, F.F., Pérez, T., Castañeda, L.F., Nava, J.L.: Mathematical modeling and simulation of electrochemical reactors: A critical review. Chemical Engineering Science **239**, 116622 (2021). DOI 10.1016/j.ces.2021.116622

[45] Sakuma, G., Fukunaka, Y., Matsushima, H.: Nucleation and growth of electrolytic gas bubbles under microgravity. International Journal of Hydrogen Energy **39**(15), 7638–7645 (2014). DOI 10.1016/j.ijhydene.2014.03.059

[46] Sander, R.: Compilation of Henry's law constants (version 4.0) for water as solvent. Atmospheric Chem. Phys. **15**(8), 4399–4981 (2015). DOI 10.5194/acp-15-4399-2015

[47] Scriven, L.E.: On the dynamics of phase growth. Chemical Engineering Science **10**(1), 1–13 (1959). DOI 10.1016/0009-2509(59)80019-1

[48] Sepahi, F., Pande, N., Chong, K.L., Mul, G., Verzicco, R., Lohse, D., Mei, B.T., Krug, D.: The effect of buoyancy driven convection on the growth and dissolution of bubbles on electrodes. Electrochimica Acta **403**, 139616 (2022). DOI 10.1016/j.electacta.2021. 139616

[49] Soto, Á.M., German, S.R., Ren, H., van der Meer, D., Lohse, D., Edwards, M.A., White, H.S.: The Nucleation Rate of Single O_2 Nanobubbles at Pt Nanoelectrodes. Langmuir **34**(25), 7309–7318 (2018). DOI 3

[50] Stewart, K., Lair, L., De La Torre, B., Phan, N.L., Das, R., Gonzalez, D., Lo, R.C., Yang, Y.: Modeling and Optimization of an Alkaline Water Electrolysis for Hydrogen Production. In: 2021 IEEE Green Energy Smart Syst. Conf. IGESSC, pp. 1–6. IEEE, Long Beach, CA, USA (2021). DOI 10.1109/IGESSC53124.2021.9618679

[51] Sussman, M., Smereka, P., Osher, S.: A Level Set Approach for Computing Solutions to Incompressible Two-Phase Flow. Journal of Computational Physics **114**(1), 146–159 (1994). DOI 10.1006/jcph.1994.1155

[52] Swiegers, G.F., Terrett, R.N.L., Tsekouras, G., Tsuzuki, T., Pace, R.J., Stranger, R.: The prospects of developing a highly energy-efficient water electrolyser by eliminating or mitigating bubble effects. Sustainable Energy Fuels **5**(5), 1280–1310 (2021). DOI 10.1039/D0SE01886D

[53] Taqieddin, A., Allshouse, M.R., Alshawabkeh, A.N.: Editors' Choice—Critical Review—Mathematical Formulations of Electrochemically Gas-Evolving Systems. J. Electrochem. Soc. **165**(13), E694 (2018). DOI 10.1149/2.0791813jes

[54] Taqieddin, A., Nazari, R., Rajic, L., Alshawabkeh, A.: Review—Physicochemical Hydrodynamics of Gas Bubbles in Two Phase Electrochemical Systems. J. Electrochem. Soc. **164**(13), E448 (2017). DOI 10.1149/2.1161713jes

[55] Vachaparambil, K.J., Einarsrud, K.E.: Numerical simulation of bubble growth in a supersaturated solution. Applied Mathematical Modelling **81**, 690–710 (2020). DOI 10.1016/j.apm.2020.01.017

[56] Vachaparambil, K.J., Einarsrud, K.E.: Numerical simulation of continuum scale electrochemical hydrogen bubble evolution. Applied Mathematical Modelling **98**, 343–377 (2021). DOI 10.1016/j.apm.2021.05.007

[57] van der Linde, P., Moreno Soto, Á., Peñas-López, P., Rodríguez-Rodríguez, J., Lohse, D., Gardeniers, H., van der Meer, D., Fernández Rivas, D.: Electrolysis-Driven and Pressure-Controlled Diffusive Growth of Successive Bubbles on Microstructured Surfaces. Langmuir **33**(45), 12873–12886 (2017). DOI 10.1021/acs.langmuir.7b02978

[58] van der Linde, P., Peñas-López, P., Moreno Soto, Á., van der Meer, D., Lohse, D., Gardeniers, H., Fernández Rivas, D.: Gas bubble evolution on microstructured silicon substrates. Energy Environ. Sci. **11**(12), 3452–3462 (2018). DOI 10.1039/C8EE02657B

[59] Verhallen, P.T.H.M., Oomen, L.J.P., v. d. Elsen, A.J.J.M., Kruger, J., Fortuin, J.M.H.: The diffusion coefficients of helium, hydrogen, oxygen and nitrogen in water determined from the permeability of a stagnant liquid layer in the quasi-s. Chemical Engineering Science **39**(11), 1535–1541 (1984). DOI 10.1016/0009-2509(84)80082-2

[60] Vogt, H.: The incremental ohmic resistance caused by bubbles adhering to an electrode. J Appl Electrochem **13**(1), 87–88 (1983). DOI 10.1007/BF00615891

[61] Vogt, H.: The problem of the departure diameter of bubbles at gas-evolving electrodes. Electrochimica Acta **34**(10), 1429–1432 (1989). DOI 10.1016/0013-4686(89)87183-X

[62] Vogt, H.: The Concentration Overpotential of Gas Evolving Electrodes as a Multiple Problem of Mass Transfer. J. Electrochem. Soc. **137**(4), 1179 (1990). DOI 10.1149/1. 2086624

[63] Vogt, H., Balzer, R.: The bubble coverage of gas-evolving electrodes in stagnant electrolytes. Electrochimica Acta **50**(10), 2073–2079 (2005). DOI 10.1016/j.electacta.2004. 09.025

[64] Vogt, H., Stephan, K.: Local microprocesses at gas-evolving electrodes and their influence on mass transfer. Electrochimica Acta **155**, 348–356 (2015). DOI 10.1016/j. electacta.2015.01.008

[65] Wang, Y., Gordon, E., Ren, H.: Mapping the Nucleation of H $_2$ Bubbles on Polycrystalline Pt via Scanning Electrochemical Cell Microscopy. J. Phys. Chem. Lett. **10**(14), 3887–3892 (2019). DOI 10.1021/acs.jpclett.9b01414

[66] Westerheide, D.E., Westwater, J.W.: Isothermal growth of hydrogen bubbles during electrolysis. AIChE J. **7**(3), 357–362 (1961). DOI 10.1002/aic.690070303

[67] Wosiak, G., da Silva, J., Sena, S.S., de Andrade, R.N., Pereira, E.: CFD simulation and experimental comparison of bubble-induced convection during electrochemical water splitting. Chemical Engineering Journal **433**, 133194 (2022). DOI 10.1016/j.cej.2021. 133194

[68] Yan, R., Pham, R., Chen, C.L.: Activating Bubble's Escape, Coalescence, and Departure under an Electric Field Effect. Langmuir **36**(51), 15558–15571 (2020). DOI 10.1021/acs.langmuir.0c02903

[69] Yang, X., Baczyzmalski, D., Cierpka, C., Mutschke, G., Eckert, K.: Marangoni convection at electrogenerated hydrogen bubbles. Phys. Chem. Chem. Phys. **20**(17), 11542–11548 (2018). DOI 10.1039/C8CP01050A

[70] Yang, X., Karnbach, F., Uhlemann, M., Odenbach, S., Eckert, K.: Dynamics of Single Hydrogen Bubbles at a Platinum Microelectrode. Langmuir **31**(29), 8184–8193 (2015). DOI 10.1021/acs.langmuir.5b01825

[71] Yuan, H.Z., Shu, C., Wang, Y., Shu, S.: A simple mass-conserved level set method for simulation of multiphase flows. Phys. Fluids **30**(4), 040908 (2018). DOI 10.1063/1. 5010152

[72] Zarghami, A., Deen, N.G., Vreman, A.W.: CFD modeling of multiphase flow in an alkaline water electrolyzer. Chemical Engineering Science **227**, 115926 (2020). DOI 10.1016/j.ces.2020.115926

[73] Zhan, S., Yuan, R., Huang, Y., Zhang, W., Li, B., Wang, Z., Wang, J.: Numerical simulation of hydrogen bubble growth and mass transfer on horizontal microelectrode surface under electrode-normal magnetic field. Physics of Fluids **34**(11), 112120 (2022). DOI 10.1063/5.0127299

Highlights

Investigating Mass Transfer Around Spatially-Decoupled Electrolytic Bubbles

Akash Raman, Carla Corina dos Santos Porto, Han Gardeniers, Cíntia Soares, David Fernández Rivas, Natan Padoin

- Simulation of successive spatially electrolytic bubbles using moving mesh method
- Bubble departures aid the formation of a pseudo-steady concentration profile
- Bubbles outgrow the region of saturated electrolyte for the currents considered
- Hydrogen dissolves from apex of bubbles exposed to undersaturated electrolyte
- Outward flux of hydrogen at the apex of the bubble limits gas-evolution efficiency

Declaration of interests

☒ The authors declare that they have no known competing financial interests or personal relationships that could have appeared to influence the work reported in this paper.

☐ The authors declare the following financial interests/personal relationships which may be considered as potential competing interests: